J|A|C|S
A R T I C L E S

Amphiphilic Poly(phenyleneethynylene)s Can Mimic Antimicrobial Peptide Membrane Disordering Effect by Membrane Insertion

Yuji Ishitsuka,[†] Lachelle Arnt,[‡] Jaroslaw Majewski,[§] Shelli Frey,[†] Maria Ratajczek,[†] Kristian Kjaer,[||] Gregory N. Tew,[‡] and Ka Yee C. Lee*,[†]

Contribution from the Department of Chemistry, the Institute for Biophysical Dynamics & the James Franck Institute, the University of Chicago, Chicago, Illinois 60637, Department of Polymer Science and Engineering, University of Massachusetts, Amherst, Amherst, Massachusetts 01003, Manuel Lujan, Jr. Neutron Scattering Center, Los Alamos National Laboratory, Los Alamos, New Mexico 87545, and Materials Research Department, Niels Bohr Institute, University of Copenhagen, DK-2100 Copenhagen, Denmark

Received March 1, 2006; E-mail: kayeelee@uchicago.edu.

Abstract: Antimicrobial peptides (AMPs) are a class of peptides that are innate to various organisms and function as a defense agent against harmful microorganisms by means of membrane disordering. Characteristic chemical and structural properties of AMPs allow selective interaction and subsequent disruption of invaders' cell membranes. Polymers based on *m*-phenylene ethynylenes (mPE) were designed and synthesized to mimic the amphiphilic, cationic, and rigid structure of AMPs and were found to be good mimics of AMPs in terms of their high potency toward microbes and low hemolytic activities. Using a Langmuir monolayer insertion assay, two mPEs are found to readily insert into anionic model bacterial membranes but to differ in the degree of selectivity between bacterial and mammalian erythrocyte model membranes. Comparison of grazing incidence X-ray diffraction (GIXD) data before and after the insertion of mPE clearly indicates that the insertion of mPE disrupts lipid packing, altering the tilt of the lipid tail. X-ray reflectivity (XR) measurements of the lipid/mPE system demonstrate that mPE molecules insert through the headgroup region and partially into the tail group region, thus accounting for the observed disordering of tail packing. This study demonstrates that mPEs can mimic AMP's membrane disordering.

Introduction

Antimicrobial peptides (AMPs) have recently attracted considerable attention because of their broad spectrum activity and potential use as new antibiotics.[1,2] They are particularly interesting as they appear to target lipid bilayers rather than specific protein receptors. Although there are over 700 different sequences known,[3] a common characteristic is that many of them adopt a cationic and amphiphilic structure. Two illustrative examples include α-helical magainin and β-sheet protegrin-1 (PG-1).[4,5] Both peptides fold into secondary structures that concentrate cationic charges and nonpolar groups into specific locations. Magainin creates two surfaces that are diametrically opposed which we refer to as facially amphiphilic, while PG-1 localizes cationic charges at the ends with nonpolar groups concentrated in the middle. It is this balance of cationic and nonpolar groups that appear to be responsible for their ability to kill bacteria selectively through membrane disruption.[1]

To better understand structure−property relationships of these peptides, a number of research efforts have focused on non-natural molecules that aim to capture the essential bioactivity. These include structures that are quite similar in chemical composition to AMPs such as stereoisomers of natural peptides,[6−8] β-peptides,[9−13] cyclic α-peptides,[14] and peptoids.[15] Many α-peptides, β-peptides, and peptoids also mimic the

[†] University of Chicago.
[‡] University of Massachusetts.
[§] Los Alamos National Laboratory.
[||] University of Copenhagen.

(1) Zasloff, M. *Nature* **2002**, *415* (6870), 389−395.
(2) Shai, Y. *Biopolymers* **2002**, *66* (4), 236−248.
(3) Tossi, A.; Sandri, L.; Giangaspero, A. *Biopolymers* **2000**, *55* (1), 4−30.
(4) Zasloff, M.; Martin, B.; Chen, H. C. *Proc. Natl. Acad. Sci. U.S.A* **1988**, *85* (3), 910−913.
(5) Kokryakov, V. N.; Harwig, S. S.; Panyutich, E. A.; Shevchenko, A. A.; Aleshina, G. M.; Shamova, O. V.; Korneva, H. A.; Lehrer, R. I. *FEBS Lett.* **1993**, *327* (2), 231−236.
(6) Wade, D.; Boman, A.; Wahlin, B.; Drain, C. M.; Andreu, D.; Boman, H. G.; Merrifield, R. B. *Proc. Natl. Acad. Sci. U.S.A* **1990**, *87* (12), 4761−4765.
(7) Oren, Z.; Shai, Y. *Biochemistry* **1997**, *36*, 6 (7), 1826−1835.
(8) Dathe, M.; Schumann, M.; Wieprecht, T.; Winkler, A.; Beyermann, M.; Krause, E.; Matsuzaki, K.; Murase, O.; Bienert, M. *Biochemistry* **1996**, *35*, 5 (38), 12612−12622.
(9) Raguse, T. L.; Porter, E. A.; Weisblum, B.; Gellman, S. H. *J. Am. Chem. Soc.* **2002**, *124* (43), 12774−12785.
(10) Porter, E. A.; Wang, X.; Lee, H. S.; Weisblum, B.; Gellman, S. H. *Nature* **2000**, *405* (6784), 298−298.
(11) Porter, E. A.; Weisblum, B.; Gellman, S. H. *J. Am. Chem. Soc.* **2002**, *124* (25), 7324−7330.
(12) Liu, D. H.; DeGrado, W. F. *J. Am. Chem. Soc.* **2001**, *123* (31), 7553−7559.
(13) Hamuro, Y.; Schneider, J. P.; DeGrado, W. F. *J. Am. Chem. Soc.* **1999**, *121* (51), 12200−12201.
(14) Fernandez-Lopez, S.; Kim, H. S.; Choi, E. C.; Delgado, M.; Granja, J. R.; Khasanov, A.; Kraehenbuehl, K.; Long, G.; Weinberger, D. A.; Wilcoxen, K. M.; Ghadiri, M. R. *Nature* **2001**, *412* (6845), 452−455.
(15) Patch, J. A.; Barron, A. E. *J. Am. Chem. Soc.* **2003**, *125* (40), 12092−12093.

helical structure found in AMPs such as magainin. To push the structure−property relationships even further, the decoration of aromatic backbones, including arylamides[16−18] and phenylene ethynylenes,[19] with cationic groups has led to structures which possess both antibacterial activity and the ability to discriminate prokaryotic from eukaryotic mammalian red blood cells (RBCs). These and other studies confirm that the presence of a defined secondary structure is not essential to antimicrobial activity[7,16−22]. This is also the case with oligo *m*-phenylene ethynylenes (mPE) based molecules. The mPE based molecules show antimicrobial activity that resembles natural peptides despite their abiogenic nature and their backbone lacking proteolytic amide bonds and chiral centers. However, little is known about how they interact with membranes and how they kill bacterial cells.

Natural AMPs have an amazing ability to discriminate prokaryotic from eukaryotic cells, believed to result from the significant differences in the lipid compositions of the cells.[1] For example, the outer leaflet of mammalian membranes is composed mainly of neutral phosphatidylcholine (PC), sphingomyelin, and cholesterol, while bacterial membranes have a significant population of anionic phosphatidylglycerol (PG) and lipopolysaccharide as well as cardiolipin.[23] However, the ability to discriminate between lipids is more subtle than simple charge effects. Magainin was shown to interact preferentially with PG over phosphatidylserine although both lipids have an equal net charge of −1.[24] Similarly, PG-1 was shown to significantly disorder zwitterionic PC monolayers but only marginally affect zwitterionic phosphatidylethanolamine.[25,26] To better understand the basic interactions of these biomimetic structures with membranes, we have initiated a systematic study using both model and live membrane systems.

We report here results for two mPEs (see Figure 1). The overall design consideration for these mPEs was to capture the cationic amphiphilic nature of AMPs using entirely abiotic backbones. One sample, compound **1**, was prepared through polymerization techniques and therefore has significant molecular weight variation. The appropriate design of these polydisperse structures led to nonhemolytic, antibacterial activity.[19] A discrete molecular weight structure, compound **2**, was prepared and found to be more potent and selective than the larger **1**. In addition to the overall facially amphiphilic structure,[19,27,28] the discrete oligomer **2** has additional similarities to PG-1. As shown in Figure 1, **2** has cationic charges confined to the two ends bridged by a hydrophobic domain in the middle. The structure−
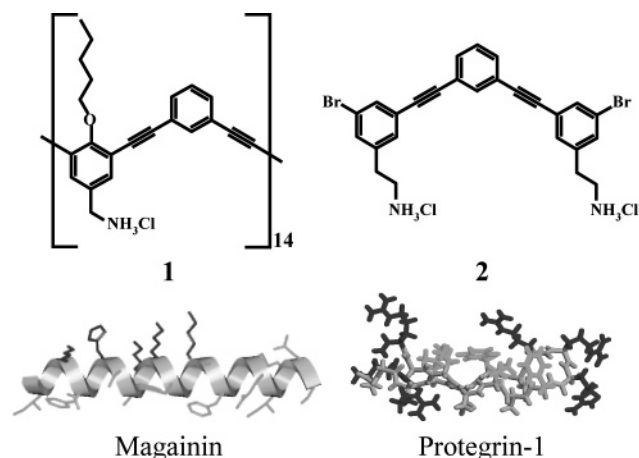

Figure 1. Chemical structures of mPEs and molecular models of AMPs. For maganin, residues with hydrophilic (dark gray) and hydrophobic (light gray) side chains are on opposite sides of the helix, giving rise to an amphiphilic structure; for PG-1, the cationic amino acids (dark gray) flank both ends of the peptide.

property relationship of these two structures has been studied previously.[19,29,30] These two structures are chosen for the present study as they span the activity range.

Various analytical techniques have been used to elucidate antimicrobial peptide-membrane interactions. For instance, interactions between antimicrobial peptide PG-1 and lipid membranes have been studied using vesicle rupture assay,[31] oriented circular dichroism,[32] lamellar X-ray diffraction,[33] atomic force microscopy,[34] solid-state nuclear magnetic resonance,[35] and computational sequence analysis.[36] The mPE−membrane interactions also have been studied using liposome rupture assay, small-angle X-ray scattering,[29] and, most recently, sum frequency generation vibrational spectroscopy has been used to study similar mimics.[37] While these techniques help elucidate the overall effect of mPE molecules on the membrane system, Langmuir monolayer insertion assay, X-ray reflectivity (XR), and grazing incidence X-ray diffraction (GIXD) have never been used in concert to obtain information of mPE−membrane interactions at the molecular level. Our work shows that these two mPE molecules insert preferentially into DPPG compared to DPPC monolayers. The smaller molecule, **2**, inserts to a greater degree than **1**, consistent with **2** exhibiting higher activity during in vitro experiments. GIXD shows that mPEs disrupt lipid ordering, and XR identifies, for the first time, the location of these cationic molecules within the membrane.

(16) Tang, H. Z.; Doerksen, R. J.; Tew, G. N. *Chem. Commun.* **2005**, (12), 1537−1539.
(17) Tew, G. N.; Liu, D.; Chen, B.; Doerksen, R. J.; Kaplan, J.; Carroll, P. J.; Klein, M. L.; DeGrado, W. F. *Proc. Natl. Acad. Sci. U.S.A* **2002**, *99* (8), 5110−5114.
(18) Liu, D. H.; Choi, S.; Chen, B.; Doerksen, R. J.; Clements, D. J.; Winkler, J. D.; Klein, M. L.; DeGrado, W. F. *Angew. Chem., Int. Ed.* **2004**, *43* (9), 1158−1162.
(19) Arnt, L.; Nusslein, K.; Tew, G. N. *J. Polym. Sci. Part A: Polym. Chem.* **2004**, *42* (15), 3860−3864.
(20) Papo, N.; Shahar, M.; Eisenbach, L.; Shai, Y. *J. Biol. Chem.* **2003**, *278* (23), 21018−21023.
(21) Papo, N.; Shai, Y. *Biochemistry* **2003**, *42* (31), 9346−9354.
(22) Schmitt, M. A.; Weisblum, B.; Gellman, S. H. *J. Am. Chem. Soc.* **2004**, *126* (22), 6848−6849.
(23) Graham, J. M. *Membrane Analysis*; Springer: New York, 1997.
(24) Matsuzaki, K.; Sugishita, K.; Ishibe, N.; Ueha, M.; Nakata, S.; Miyajima, K.; Epand, R. M. *Biochemistry* **1998**, *37*, 7 (34), 11856−11863.
(25) Gidalevitz, D.; Ishitsuka, Y.; Muresan, A. S.; Konovalov, O.; Waring, A. J.; Lehrer, R. I.; Lee, K. Y. C. *Proc. Natl. Acad. Sci. U.S.A.* **2003**, *100* (11), 6302−6307.
(26) Ishitsuka, Y.; Pham, D.; Waring, A. J.; Lehrer, R. I.; Lee, K. Y. C. *Biochim. Biophys. Acta* doi:10.1016/.j.bbamem.r006.08.001.

(27) Arnt, L.; Tew, G. N. *J. Am. Chem. Soc.* **2002**, *124* (26), 7664−7665.
(28) Arnt, L.; Tew, G. N. *Langmuir* **2003**, *19* (6), 2404−2408.
(29) Arnt, L.; Rennie, J. R.; Linser, S.; Willumeit, R.; Tew, G. N. *J. Phys. Chem. B* **2006**, *110* (8), 3527−3532.
(30) Tew, G. N.; Clements, D.; Tang, H.; L., A.; Scott, R. W. *Biochim. Biophys. Acta*, in press.
(31) Waring, A. J.; Harwig, S. S. L.; Lehrer, R. L. *Protein Pept. Lett.* **1996**, *3*, (3), 177−184.
(32) Heller, W. T.; Waring, A. J.; Lehrer, R. I.; Huang, H. W. *Biochemistry* **1998**, *37*, 7 (49), 17331−17338.
(33) Heller, W. T.; Waring, A. J.; Lehrer, R. I.; Harroun, T. A.; Weiss, T. M.; Yang, L.; Huang, H. W. *Biochemistry* **2000**, *39* (1), 139−145.
(34) Lam, K. L.; Ishitsuka, Y.; Y., C.; K., C.; Waring, A. J.; Lehrer, R. L.; Lee, K. Y. C. *J. Phys. Chem. B*, in press.
(35) Marasinghe, P. A. B.; Buffy, J. J.; Schmidt-Rohr, K.; Hong, M. *J. Phys. Chem. B* **2005**, *109* (46), 22036−22044.
(36) Ostberg, N.; Kaznessis, Y. *Peptides* **2005**, *26* (2), 197−206.
(37) Chen, X. Y.; Tang, H. Z.; Even, M. A.; Wang, J.; Tew, G. N.; Chen, Z. *J. Am. Chem. Soc.* **2006**, *128* (8), 2711−2714.

Materials and Methods

Antimicrobial Testing. All experiments were performed according to standard procedures.[19,38] Briefly, **1** and **2** in dimethyl sulfoxide (molecular biology grade, Fisher Scientific, Pittsburgh, PA) stock solutions at 140 μg/mL were diluted into 96-well plates with Mueller Hinton medium to a constant volume of 150 μL following a 2-fold dilution series.[38] *Escherichia coli* D31 and methicillin-resistant *Staphylococcus aureus* OC2878 were used as test organisms starting with the optical density of the medium at 600 nm (OD_{600}) of 0.001 (approximately 10^5 cells/mL). Antibacterial activity was measured after incubation at 37 °C for 20 h by determining the OD_{600} of each well using a Molecular Probes SpectraMax 190 plate reader. The reported, minimum inhibitory concentration (MIC) values are the minimum concentrations necessary to inhibit >90% of cell growth compared to a control sample without antibacterial agent. All reported values represent a minimum of quadruplicate experiments. The reduction in cell count by OD_{600} was confirmed by serial 10-fold dilutions followed by spreading the bacteria onto agar plates and incubating overnight at 37 °C to confirm the MIC.

Hemolysis Assay. Hemolysis samples were prepared according to standard procedures.[19,38] Briefly, 80 μL of RBCs suspended in TRIS buffer and ~20 μL of buffer containing the antibacterial agent were placed into 96-well plates. The total volume was held constant at 100 μL. After incubation for 30 min at 37 °C, an aliquot of the supernatant was diluted with buffer, and the optical density of the medium at 414 nm, OD_{414}, was measured to quantify release of hemoglobin. Complete hemolysis was measured by adding 1% Triton X-100 to the RBCs and incubating for 30 min. The HC_{50}, the 50% hemolytic concentration, is reported. Therefore, the selectivity values reported for **2** represent a conservative estimate by comparing MIC for >90% inhibition to HC_{50}.

Lipid Solution Preparation. DPPC and DPPG were purchased (Avanti Polar Lipids, Inc.) and used without further purification. DPPC powder was dissolved in chloroform, and DPPG powder was dissolved in 1:9 methanol/chloroform by volume (Fisher Scientific).

Preparation of 1 and 2. Molecule **1** ($M_r = 4770$) is on average composed of 14 monomers while **2** ($M_r = 590$) is a single compound. Synthetic procedures for **1** and **2** have been published elsewhere.[27] Stock solutions were prepared by dissolving **1** or **2** in dimethyl sulfoxide to make up a concentration of 7 and 4 mg/mL, respectively. The stock solution of **1** was diluted in chloroform to 0.3 mg/mL, and that of **2** was diluted in a 23:77 methanol/chloroform solution to 0.2 mg/mL. For constant surface pressure insertion experiments, the same stock solutions were further diluted by buffer just prior to injection into the subphase.

Langmuir Surface Balance. A Langmuir monolayer provides a good mimic for the outer leaflet of the cell membrane. A home-built Langmuir surface balance was used for all surface pressure (Π)–surface area (A) measurements.[39] In brief, our apparatus consists of a Teflon trough with two symmetric, movable barriers that control the monolayer area. A Wilhelmy plate made of filter paper is used to measure the change in Π accompanied by the change in surface area. Π is the difference in surface tension between a pure subphase and one with a monolayer adsorbed. The temperature is maintained by a series of thermoelectric heating/cooling units (Omega Engineering, Inc.), and a resistively heated indium tin oxide coated glass plate (Delta Technologies) is placed over the trough to minimize evaporation, convection, and contamination. The setup is controlled by a software interface designed using Lab View 6.0 (National Instruments).

Constant Pressure Insertion Studies. To quantify the interaction of mPEs with lipid monolayers, we have carried out constant pressure insertion studies. DPPC and DPPG monolayers were spread dropwise at the air–buffer interface using a microsyringe (Hamilton). After solvent evaporation, the monolayer was compressed to $\Pi = 30$ mN/m, a bilayer equivalent pressure.[40] Π was kept constant via a built-in feedback system that adjusts the surface area, A. Unless stated otherwise, experiments were carried out on Dulbecco's phosphate-buffered saline, without any calcium or magnesium (DPBS; Invitrogen) at 30 ± 0.5 °C. The calculated electron density of DPBS, ρ_{DPBS}, from the known salt content is 0.33645 Å^{-3}. The mPE was evenly injected underneath the monolayer using a microsyringe (VDRL needle; Hamilton) to make up the final concentration of 6.1 μM. This concentration was chosen to allow for direct comparison with results from our previous work on **1** with liposomes.[28] The final subphase molar concentrations of **1** and **2** were kept constant for insertion assay experiments. Injected polymers interact with the lipid monolayer and result in an increase in Π. To keep Π constant, the area has to increase. The resulting relative area change, $\Delta A/A$, was monitored to compare the degree of mPE insertion into DPPC and DPPG monolayers.

XR and GIXD. In a typical experiment, the trough canister is flushed with He (at least 30 min) after the monolayer is spread, achieving an oxygen level below 1%. This both minimizes oxidative damage and reduces background scattering. The monolayer is then compressed to the desired Π before XR and GIXD are carried out to obtain out-of-plane and in-plane structural information of these samples, respectively. As an added precaution against beam damage, the trough is translated laterally 0.025 mm across the beam at every step of the GIXD scan, while during XR, the sample is occasionally renewed completely by translating the full 2 mm width of the beam.

The types of information obtainable by GIXD and XR are reviewed in depth elsewhere.[41,42] XR yields detailed information on the electron density distribution normal to the interface, $\rho_{el}(z)$, laterally averaged over both the ordered and disordered parts of the film. In our analysis, a slab model is used in which the monolayer is represented as a stack of slabs, each slab having a constant ρ_{el} and thickness, t. The interfaces between slabs are smeared out by convolution with a Gaussian function of rms width σ to account for roughness at the boundary because of thermally excited capillary waves as well as additional local interfacial diffuseness.[42,43] XR data therefore allow us to determine the vertical location of the mPE with respect to the lipids.

In GIXD, the scattered intensity is measured by scanning over a range of horizontal scattering vector components: $Q_{xy} \approx 2\pi/\lambda \sqrt{1 + \cos^2 \alpha_f - \cos 2\theta_{xy}}$ where $2\theta_{xy}$ is the angle between the incident and diffracted beams projected on the liquid surface.[41] Bragg peaks, resolved in Q_{xy}, are obtained by integrating the scattered intensity over all channels in the position sensitive detector that is perpendicular to the interface (i.e., along $Q_z = 2\pi/\lambda (\sin \alpha_i + \sin \alpha_f) \approx 2\pi/\lambda \sin \alpha_f$). Conversely, the Bragg rod profiles are obtained by integrating, after background subtraction, for each position sensitive detector channel, the scattered intensity across a Bragg peak. The angular positions of the Bragg peaks determine the *d*-spacings $d_{hk} = 2\pi/Q_{xy}$ for the 2D lattice. From the line widths of the peaks, it is possible to determine the 2D crystalline coherence length L_{xy} (the average distance over which crystallinity extends). The intensity distribution along the Bragg rod can be analyzed to determine the direction and magnitude of the molecular tilt, the out-of-plane coherence length L_c (the length of the molecule which scatters coherently), and the surface roughness of the crystallite (Debye–Waller factor).

(38) NCCLS, NCCLS standards. National Committee for Clinical Laboratory Standards. *M7-A6, Methods for Dilution Antimicrobial Susceptibility Tests for Bacteria that Grow Aerobically; Approved Standard,* 6th ed.; National Committee for Clinical Laboratory Standards: Wayne, PA, January, 2003.

(39) Gopal, A.; Lee, K. Y. C. *J. Phys, Chem. B* **2001**, *105* (42), 10348–10354.

(40) Seelig, A. *Biochim. Biophys. Acta* **1987**, *899* (2), 196–204.

(41) Jensen, T. R.; Kjaer, K. Structural properties and interactions of thin films at the air–liquid interface explored by synchrotron X-ray scattering. In *Novel Methods To Study Interfacial Layers*; Mobius, D., Miller, R., Eds.; Studies in Interface Science, Vol. 11; Elsevier: Amsterdam, The Netherlands, 2001; p 205.

(42) Als-Nielsen, J.; Jacquemain, D.; Kjaer, K.; Leveiller, F.; Lahav, M.; Leiserowitz, L. *Phys. Rep., Rev. Sect. Phys. Lett.* **1994**, *246* (5), 252–313.

(43) Als-Nielsen, J.; Kjaer, K. Phase Transitions in Soft Condensed Matter. In Riste, T., Sherrington, D., Eds.; Plenum Press: New York, 1989; p 113.
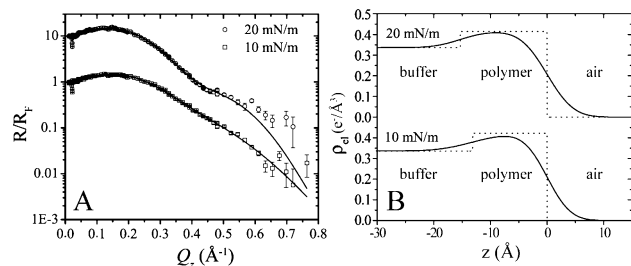
Figure 2. (A) XR of **1** monolayers at 10 and 20 mN/m, and (B) their corresponding model density profile. Solid line for panel A is the best fit using one box model. Solid and dashed lines for panel B are smeared and unsmeared $\rho_{el}(z)$ profiles of data in panel A, respectively.

Results and Discussion

Antibacterial and Hemolysis Results. The antibacterial and hemolytic activity of **1** and **2** were tested using standard microbroth dilution protocols to determine their MIC and HC$_{50}$. In accordance with previous findings,[19,38] **1** was relatively nonpolar and no antibacterial activity was measured up to 100 μg/mL, beyond which solubility became an issue. By contrast, the much smaller compound, **2**, exhibited potent activity against both gram-negative *E. coli* and gram-positive methicillin resistant *S. aureus* with an MIC of 0.8 and 0.5 μg/mL, respectively. In comparison to these MIC values, HC$_{50}$ of **2** (75 μg/mL) showed 94 and 155-fold selectivity of prokaryotes over eukaryotes, respectively. Comparison of the HC$_{50}$ and MIC values shows that **2** is significantly more active toward bacteria than RBCs.

mPE Monolayers. Compound **1** formed a stable monolayer at the air-buffer interface and XR measurements were carried out at 10 and 20 mN/m (Figure 2). A single slab representing the entire polymer monolayer produced the best fit for both data sets. At 10 mN/m, the ρ_{el} of the polymer layer was 0.421 $\pm$ 0.003 e$^-$/Å^3 with a layer thickness of 13.1 $\pm$ 0.3 Å. Two values of surface roughness for the subphase-polymer (σ_{S-P}; 4.8 $\pm$ 0.2 Å) and the polymer-air (σ_{P-A}; 3.28 $\pm$ 0.03 Å) interfaces were used to account for the two interfaces. At 20 mN/m, the fit gave a similar ρ_{el} value of 0.414 $\pm$ 0.003 e$^-$/Å^3, but the thickness increased to 15.34 $\pm$ 0.09 Å, with a single roughness of 3.68 $\pm$ 0.01 Å. A layer thickness of 13−15 Å agrees well with predictions from molecular models and powder X-ray diffraction.[44] GIXD measurements were performed at both pressures but no diffraction peaks were observed for either case, indicating the lack of any in-plane ordering.

Compound **2** was designed and synthesized both to enhance water solubility and to allow increased control over molecular size. As a result, it does not form a stable monolayer at the air-buffer interface as indicated by the absence of change in Π upon compression.

Insertion of 1 into DPPC and DPPG Monolayers. Constant pressure insertion studies of **1** with DPPC and DPPG monolayers in conjunction with XR and GIXD measurements were performed at 30 mN/m to investigate its membrane selectivity, the location of the inserted **1** in the lipid matrix, as well as its membrane disordering effect, respectively.

$\Delta A/A$ values obtained after the injection of **1** were significantly different between DPPC and DPPG, demonstrating the membrane selectivity of **1**. While the maximum $\Delta A/A$ was
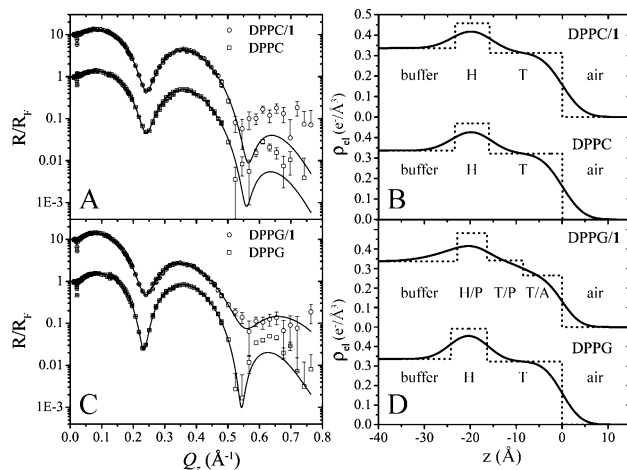
(44) Kim, T.; Arnt, L.; Atkins, E.; Tew, G. N. *Chem. Eur. J.* **2006**, *12*, 2423−2427.

Figure 3. XR and the corresponding electron density, $\rho_{el}(z)$, profile of DPPC and DPPC/**1** (A and B) and DPPG and DPPG /**1** (C and D) at 30 mN/m. Solid lines for panels A and C are the best fits of the models to the experimental data. Solid and dashed lines for panels B and D are smeared and unsmeared $\rho_{el}(z)$ profiles of corresponding XR curves, respectively.

merely 2% for the model mammalian membrane DPPC, a $\Delta A/A$ equal to 19% was observed for the model bacterial membrane DPPG.

The different degrees of insertion are also reflected by changes in the XR curves of DPPC and DPPG before and after the injection of **1** (Figure 3). XR curves normalized by Fresnel reflectivity are shown in Figure 3A,C, with their corresponding ρ_{el} profiles fitting in Figure 3B,D. Zero on the *x*-axis is chosen at the boundary between the tail and air, with the solid and dashed lines indicating the smeared and unsmeared $\rho_{el}(z)$ profiles, respectively. For clarity, all XR data, corresponding fitted curves, ρ_{el} profile, and corresponding slab models have been offset vertically. All XR fit parameters are in Table 1. Both DPPC and DPPG monolayers were fitted using a two-slab model by varying the density $\rho_{el(i)}$, thickness $t_{(i)}$ and surface roughness $\sigma_{(i)}$ for each slab (i). Both sets of data have also been fitted using a three-slab model, but the fits reverted back to those obtained using a two-slab model. The final fit was achieved by minimizing the χ-square value while ensuring that parameters obtained were physically meaningful.

For insertion of **1** into a DPPC monolayer, only a minute change is observed in the XR curves before and after polymer injection (Figure 3A,B), indicating a weak interaction. The XR curve for the DPPC/**1** system can be fitted using a two-slab model (headgroup (H) and tail group (T)), showing only minor thickness and roughness differences compared to pure DPPC. For DPPC, no additional slab for any adsorbed polymer (P) was necessary to fit the data after the injection of **1**, suggesting that the majority of the polymer is distributed evenly in the subphase and has a weak interaction with the DPPC film.

By contrast, a large change in the XR profile of DPPG was observed with **1** injected into the subphase (Figure 3,C,D), in agreement with the large $\Delta A/A$ observed for this system (Table 1). Because ρ_{el} of **1** at the air-buffer interface is lower than that of the lipid headgroup but higher than that of the tail, the insertion of **1** should reduce the headgroup ρ_{el} but increase that of the tail. Should the inserted **1** penetrate partially into the tail, the region could be represented by two different slabs: one with the polymer and one without. The former should have a higher ρ_{el} than that of the pure lipid tail, and ρ_{el} of the latter should go

Table 1. XR Fit Parameters[a]

	ρ_H (e⁻/Å³)	t_H (Å)	ρ_T (e⁻/Å³)	t_T (Å)	σ (Å)	A (Å²/molec)	$\Delta A/A$ (%)
DPPC	0.469 ± 0.003	7.4 ± 0.1	0.322 ± 0.003	16.0 ± 0.1	3.65	47	
DPPG	0.491 ± 0.003	7.9 ± 0.1	0.323 ± 0.003	16.3 ± 0.1	3.28	46	
DPPC/1	0.458 ± 0.003	7.5 ± 0.1	0.313 ± 0.003	15.9 ± 0.1	3.69	48	2

	$\rho_{H/P}$ (e⁻/Å³)	$t_{H/P}$ (Å)	$\rho_{T/P}$ (e⁻/Å³)	$t_{T/P}$ (Å)	$\rho_{T/a}$ (e⁻/Å³)	$t_{T/a}$ (Å)	σ (Å)	A (Å²/molec)	$\Delta A/A$ (%)
DPPC/2	0.451 ± 0.007	7 ± 1	0.36 ± 0.03	5.2 ± 0.7	0.202 ± 0.003	9.7 ± 0.5	3.22	59	25
DPPG/1	0.481 ± 0.007	6.5 ± 0.4	0.343 ± 0.007	7.9 ± 0.3	0.262 ± 0.003	8.5 ± 0.5	σ_{S-H}:6.96 σ: 3.14	55	19

	$\rho_{H1/P}$ (e⁻/Å³)	$t_{H1/P}$ (Å)	$\rho_{H2/P}$ (e⁻/Å³)	$t_{H2/P}$ (Å)	$\rho_{T/P}$ (e⁻/Å³)	$t_{T/P}$ (Å)	$\rho_{T/P}$ (e⁻/Å³)	$t_{T/a}$ (Å)	σ (Å)	A (Å²/molec)	$\Delta A/A$ (%)
DPPG/2	0.41 ± 0.02	3.2 ± 0.6	0.50 ± 0.02	5 ± 2	0.39 ± 0.01	5.7 ± 0.7	0.215 ± 0.003	11.8 ± 0.1	σ_{S-H}: 5.55 σ: 3.08	68	48

[a] Subscripts: H = head, T = tail, H/P = head/polymer, T/P = tail/polymer, T/a = tail/air, S-H = subphase/head interface

in the opposite direction, with the decrease in ρ_{el} proportional to the degree of polymer insertion.

The data have been exhaustively fitted using two-, three-, and four-slab models, but a two-slab model does not provide a good fit, and fits obtained using a four-slab model always revert to that of the three-slab model. The best fit is obtained using such a three-slab model (Figure 3C,D) to represent the headgroup, tail/polymer, and tail regions. As shown in Figure 3D, the slab corresponding to the DPPG headgroup has its ρ_{el} reduced from 0.491 (ρ_H) to 0.481 e⁻/Å³ ($\rho_{H/P}$) and its thickness reduced by 1.4 Å. While this reduction in thickness could be due to tilting of the headgroup, the substantial increase of the subphase-headgroup interfacial roughness (from 3.28 to 6.96 Å) is likely responsible for this observed change. The increase in roughness probably arises from the backbone flexibility of **1**. This backbone has a rotational barrier between aromatic rings of less than 1 kcal/mol at room temperature and is also known to fold into helical structures.[45,46] The torsional flexibility of this structure coupled with the increased roughness suggests that portions of **1** can extend into the subphase. How far does **1** penetrate into the monolayer? The second slab from the right for the DPPG/**1** ρ_{el} profile in Figure 3D (T/P) shows that the insertion extends into the lipid region, increasing ρ_{el} from 0.323 (ρ_T) to 0.343 e⁻/Å³ ($\rho_{T/P}$). While the thickness of the tail region is 16.3 Å, this tail/polymer slab is 7.9 Å. This makes for a total thickness of the inserted polymer of 14.4 Å, which agrees well with the thickness obtained from XR fit of **1**. The remainder of the tail portion, into which **1** does not penetrate, is represented by the third slab (T/a, where a stands for air). As expected, the polymer insertion acts to lower the ρ_{el} of this portion of the tail region, decreasing it from 0.323 (ρ_T) to 0.262 e⁻/Å³ ($\rho_{T/a}$).

Since we are able to form a stable monolayer of **1**, we can compare our results with estimates made from known ρ_{el} values of **1** and the phospholipid as well as the observed relative area increase upon insertion. For the DPPG/**1** case, our insertion assay shows 19% relative area increase. Assuming that the ρ_{el} of **1** is roughly that of the pure **1** monolayer at 20 mN/m, the final ρ_{el} profile may be estimated by linearly combining the original ρ_{el} values of the overlapping slabs of DPPG and **1**. Combining 81% of DPPG headgroup ρ_{el} and 19% of **1** ρ_{el} (H/P slab), 81% of tail group ρ_{el} and 19% of **1** ρ_{el} (T/P slab), and reducing the ρ_{el} of the tail group to 81% of the original value (T/a slab) give 0.477, 0.340, and 0.262 e⁻/Å³, respectively. These values are in quantitative agreement with the measured data.
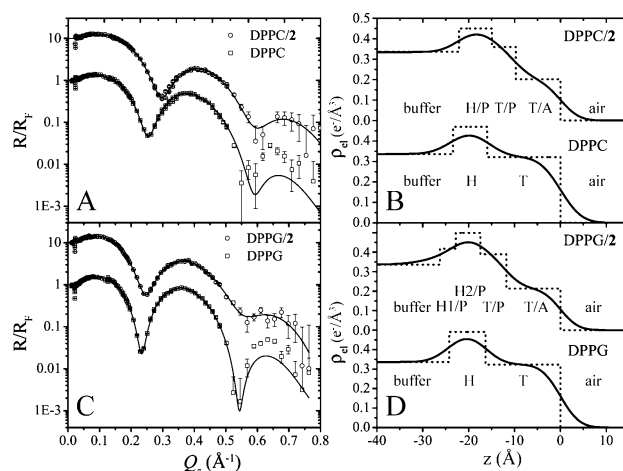
(45) Okuyama, K.; Hasegawa, T.; Ito, M.; Mikami, N. *J. Phys. Chem.* **1984**, *88* (9), 1711−1716.
(46) Nelson, J. C.; Saven, J. G.; Moore, J. S.; Wolynes, P. G. *Science* **1997**, *277* (5333), 1793−1796.

Figure 4. XR and the corresponding electron density, $\rho_{el}(z)$, profile of (A and B) DPPC and DPPC/**2** and (C and D) DPPG and DPPG/**2** at 30 mN/m. Solid lines for panels A and C are the best fits of the models to the experimental data. Solid and dashed lines for panels B and D are smeared and unsmeared $\rho_{el}(z)$ profiles of corresponding XR curves, respectively.

Insertion of 2 into DPPC and DPPG Monolayers. Constant pressure insertion studies of **2** with DPPC and DPPG monolayers followed by XR and GIXD measurements were also performed at 30 mN/m. Although the basic chemical motif of **2** is similar to that of **1**, **2** inserts significantly more into both DPPC ($\Delta A/A$ = 25%) and DPPG ($\Delta A/A$ = 48%). This corroborates our in vitro antibacterial and hemolysis results where compound **2** is significantly more active than **1**. Compound **2** also shows a higher level of insertion into DPPG than into DPPC, thus demonstrating a similar selectivity for anionic lipids. Although it is difficult to pinpoint the exact amount of membrane disruption necessary for antimicrobial activity, our insertion data for 1 and 2 should provide the lower and upper bounds, respectively, for such a threshold value.

Normalized XR data of DPPC and DPPG monolayers before and after the insertion of **2** and their corresponding fitted curves are shown in parts A and C of Figure 4, respectively; the respective fitted ρ_{el} profiles are detailed in Figure 4B,D, and all fit parameters are in Table 1. The ρ_{el} profiles after insertion of **2** are significantly different from those of the original monolayers. The overall picture obtained from the fit for DPPC/**2** is very similar to DPPG/**1**. Our data indicate that **2** inserts into the headgroup (lowering ρ_{el}, $\rho_H > \rho_{H/P}$) and into part of the tail group (increasing ρ_{el}, $\rho_T < \rho_{T/P}$), leaving the rest of the tail group loosely packed (decreasing ρ_{el}, $\rho_T > \rho_{T/a}$). Although we have fitted the data using models with a different number of slabs, the XR curve for DPPC/**2** is best fitted using three slabs. While **2** alone does not form a stable monolayer,
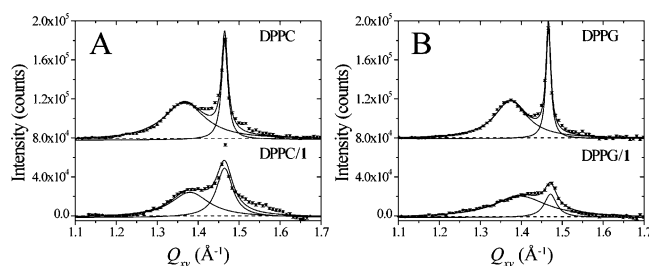
Figure 5. Bragg peaks from GIXD of (A) a DPPC monolayer and (B) a DPPG monolayer before and after insertion of **1**. Solid lines are fits for each peak. The two Bragg peaks observed indicate distorted-hexagonal packing. While **1** has little effects on the Bragg peaks of DPPC, it diminishes the peaks of DPPG, indicating the disordering of lipid packing induced by **1**.

Figure 6. Bragg peaks (A) and Bragg rods (B) from GIXD of DPPG monolayer before insertion (top) and after insertion of **2** (bottom). Solid lines are fits for each graph. For clarity, the data have been offset vertically. The two Bragg peaks observed for DPPG indicate distorted-hexagonal packing. The Miller indices {h; k} are given. The diminished peaks indicate the disordering of lipid packing induced by **2**. Bragg rod fit shows the decrease in DPPG tilt angle in the ordered domains and the reduction of coherently scattering portion of the alkyl chain.

the DPPC/**2** profile clearly shows that **2** has a high affinity toward the surface in the presence of a lipid film.

The best fit for DPPG/**2** was obtained using a four-slab model. Two- and three-slab models have been exhaustively tested but do not fit the data well. The first two slabs overlap with the headgroup while the third and fourth slabs overlap with the tail group of DPPG. As in previous cases, the decrease in ρ_{el} of the headgroup is expected from the insertion. While the first box shows a significant decrease, the second box shows an increase in the ρ_{el}. However, the combined ρ_{el} of the two is 0.464 e$^-$/Å^3, which is lower than the pure lipid headgroup ρ_{el}. From the DPPG structure, the phosphate group is the contributing factor for the high ρ_{el} of the second box. As in the case of DPPG/**1**, a larger surface roughness value is needed to fit the curve. The total thickness of **2** calculated from the insertion profile into DPPC is 12.2 Å, while that for DPPG is thicker by 1.7 Å (13.9 Å). This increase in thickness and the larger roughness for the head/subphase interface suggest that there is a staggering of the inserted molecules of **2**. Notwithstanding minor differences, the $\rho_{el}(z)$ profile for DPPC/**2** is similar to that obtained for DPPG/**2**, showing that only the degree of insertion, but not the vertical extent of penetration, is affected by headgroup electrostatics.

Lipid Disordering. The insertion assay shows that **1** and **2** insert more readily into anionic model membranes and XR provides the vertical structure of these mixed lipid and mPE films. What then is the effect of the insertion on in-plane lipid ordering? The penetration through the headgroup and the partial insertion into the tail group should affect lateral lipid packing. This effect is confirmed by our GIXD results.

Figure 5 parts A and B show the Bragg peaks of a DPPC and a DPPG monolayer, respectively, both in the absence and presence of **1**. As can be seen in Figure 5A, the Bragg peak profiles of the DPPC monolayer before and after the introduction **1** are very similar, suggesting that the presence of **1** does not significantly alter the lateral ordering of the lipid film. This finding is in line with the low level of insertion of **1** into DPPC
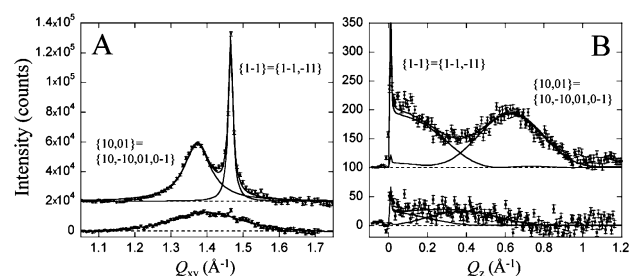
monolayers observed in our insertion assay. For the DPPG film, however, the presence of **1** results in a significant reduction in the intensity of the Bragg peaks, signifying the disordering effect of **1** on the DPPG film. Again, these results corroborate the higher level of insertion **1** has for DPPG over DPPC monolayers.

A clear example of this lateral disordering effect can be seen by comparing GIXD results of pure DPPG and DPPG/**2** monolayers (Figure 6). The summary of Bragg peak and Bragg rod analysis is shown in Table 2. Several trends in the way the inserted molecules disorders the monolayer are shared by the DPPG/**1** and DPPC/**2** systems, but the DPPG/**2** system shows a greater degree of changes because of the larger amount of insertion.

First, the integrated Bragg peak intensity decreases as a result of insertion (Figure 6A). The integrated intensity of the peak is proportional to the area of the ordered phase within the X-ray footprint. A pure DPPG monolayer, under the experimental conditions, gives rise to two Bragg peaks as the lipid chains are packed in a distorted hexagonal 2D cell. Upon mPE insertion, Bragg peaks considerably decrease in intensity. By penetrating into the tail group, mPE molecules reduce the lipid ordering that gives rise to the original Bragg peaks.

Second, the width of the Bragg peak increases upon insertion, indicative of a decrease in coherence length of the ordered domains. In the transition from DPPG to DPPG/**2**, the coherence length decreases from $L_{10,01} = 65$ Å and $L_{1-1} = 410$ Å to $L_{10,01,1-1} = 22$ Å. The insertion of mPE thus breaks up the scattering entities into domains with very short-range order.

Finally, from the Bragg rod analysis (Figure 6B) the insertion of **2** changes the tilt angle of the lipid molecule in the ordered domains and reduces the coherently scattering portion of the alkyl chain. Initially, the coherently scattering part of DPPG has a length $L_c = 18.2 \pm 1.0$ Å and a tilt angle of $30.0 \pm 0.5°$ from the surface normal. After insertion of **2**, the above

Table 2. GIXD Fit Parameters for DPPG and DPPG/2

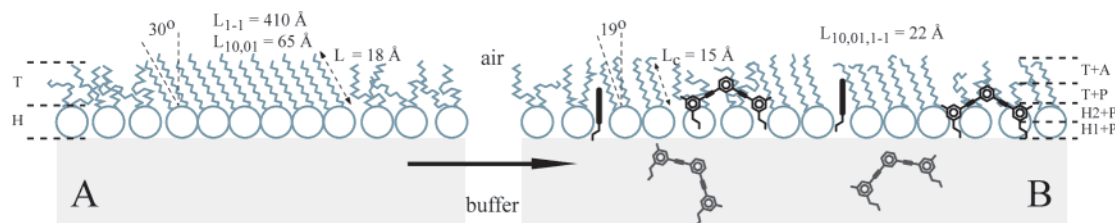| | | unit cell | | A/molec | in-plane | | coherence | tilt direction (from |
	Π	$a = b$	γ	Projected A/molec	coherence length	Tilt angle	length (L_c)	NN, nonsymmetry)
	(± 0.2 mN/m)	(± 0.01 Å)	(± 0.5°)	(Å^2/molec)	(± 5 Å)	(deg)	(± 0.5 Å)	(deg)
						in-plane Bragg peaks → out-of-plane Bragg rods		
DPPG	30	5.07	115.5	46.4 / 40.2	$L_{10,01} = 65$ / $L_{1-1} = 410$	30.0 ± 0.5	18 ± 1	10.5 ± 0.5
DPPG/2	30	5.18	120	46.5 / 44.0	$L_{10,01,1-1} = 22$	19 ± 5	15 ± 3	10 ± 5

Figure 7. Schematic showing the insertion of **2** molecules relative to lipid molecules and their disordering affect on the in-plane structure of DPPG monolayer. Panels A and B depict the situation before and after the insertion of **2** into DPPG monolayer, respectively. Upon insertion of **2** into the monolayer, DPPG ordered domains are broken into smaller patches (before: $L_{10,01} = 65$ Å and $L_{1-1} = 410$ Å; after: $L_{10,01,1-1} = 22$ Å), and the tail groups are prompted upward (before: 30°; after: 19°). **2** molecules penetrate into the headgroup region and also partially into the tail group region. The orientation of **2** is drawn such that hydrophobic portion of the molecule matches with the tail group of lipids.

parameters change to 14.7 ± 2.5 Å and $19.0 \pm 5°$, respectively. Our results clearly demonstrate that the insertion of **2** into the lower portion of the tail region pushes the alkyl chains to a more upright orientation. The fact that mPE only penetrates partially into the film also leaves room for the end of the acyl chains of the ordered domains to be loosened, thus resulting in a shorter L_c in the DPPG/**2** system. These results, taken together, show that the insertion of mPEs disorders lipid packing. The observed higher degree of membrane disordering by **2** is in line with its more potent antibacterial activities, as well as its greater ability to insert into both DPPC and DPPG monolayers.

Conclusions

The ability to design molecules that capture the essential physiochemical and biological properties of naturally occurring AMPs can lead to new insight about their fundamental modes of action and a better understanding of the key molecular aspects necessary for activity and selectivity. The mPE structures reported here represent a novel, nonbiological backbone that can be designed to produce potent nonhemolytic antibacterial compounds such as **2**. XR and GIXD experiments illustrate with near molecular resolution how these molecules insert into phospholipid monolayers and perturb the lateral packing: XR results locate the inserted molecules in the polar headgroup region and part of the nonpolar tail group, and GIXD indicates that the insertion induces lateral disordering of the monolayer (Figure 7). Although caution is always needed when extrapolating results from model studies to in vitro activity, the good agreement obtained between our model system and live cell results demonstrates that the former is effective in capturing the essence of the interaction involved and provides a platform

for dissecting this interaction at the molecular level. While both structures insert into anionic DPPG more than into zwitterionic DPPC, compound **2** is found to be more active than **1** in insertion experiments. This is in line with our in vitro experiments in which **2** has a selectivity for bacterial versus RBC of >94, whereas the activity of **1** against bacteria is so low that we are unable to determine a selectivity index. Clearly, the observed trends for in vitro activity of **1** and **2** are well correlated with their insertion ability into model lipid systems.

JA061186Q